

Label-free single-molecule detection of DNA-hybridization kinetics with a carbon nanotube field-effect transistor

Sebastian Sorgenfrei¹, Chien-yang Chiu², Ruben L. Gonzalez, Jr², Young-Jun Yu³, Philip Kim³, Colin Nuckolls² and Kenneth L. Shepard^{1*}

Single-molecule measurements of biomolecules can provide information about the molecular interactions and kinetics that are hidden in ensemble measurements. However, there is a requirement for techniques with improved sensitivity and time resolution for use in exploring biomolecular systems with fast dynamics. Here, we report the detection of DNA hybridization at the single-molecule level using a carbon nanotube field-effect transistor. By covalently attaching a single-stranded probe DNA sequence to a point defect in a carbon nanotube, we are able to measure two-level fluctuations in the conductance of the nanotube in the presence of a complementary DNA target. The kinetics of the system are studied as a function of temperature, allowing the measurement of rate constants, melting curves and activation energies for different sequences and target concentrations. The kinetics demonstrate non-Arrhenius behaviour, in agreement with DNA hybridization experiments using fluorescence correlation spectroscopy. This technique is label-free and could be used to probe single-molecule dynamics at microsecond timescales.

Studies at the single-molecule level have revealed intramolecular dynamics and conformational changes in many biomolecular systems. The intramolecular chain diffusion of nucleic acids, particularly the hairpin configuration, has been extensively studied by optical techniques such as fluorescence correlation spectroscopy (FCS)^{1–3}. In these studies, labels are attached to the DNA hairpin, and the opening and closing rates of a small number of molecules can then be monitored at submicrosecond timescales. One of the disadvantages of FCS, however, is that the observation time is limited to the diffusion time of molecules through the observation volume⁴. Single-molecule fluorescence resonance energy transfer (smFRET) has also been used to study conformational changes in biomolecules⁵, but provides timescales of only tens of milliseconds for kinetic studies. Label-free technologies for biomolecular detection include the use of nanowires⁶, microcavities⁷, mechanical cantilevers⁸, optical waveguides⁹ and optical tweezers¹⁰, but none have combined high enough sensitivity for label-free detection with the high temporal resolution necessary to monitor the kinetics of biomolecular processes on microsecond timescales.

One-dimensional conductors such as single-walled carbon nanotubes act as high-gain field-effect sensors, in which the conductance varies strongly with local charge density. However, initial experiments conducted either with specific adsorption and coated nanotubes¹¹ or non-specific adsorption with pristine nanotubes¹² have not demonstrated sufficient sensitivity to detect single biomolecules with the highest reported sensitivity for DNA detection (14 pM, ref. 12). Other studies have used carbon nanotubes as electrodes; small gaps are etched into the tubes, bridged by molecular junctions, and sensing is carried out by monitoring the conductance of the junctions. These devices are able to distinguish between fully complementary bridging DNA duplexes and those with a single mismatch; however, DNA hybridization kinetics cannot be measured¹³.

Recently it has been shown that single point defects can be electrochemically created in nanotubes in a controllable manner and can be used to covalently bind biomolecules at the scattering site¹⁴. The resultant device has been demonstrated to exhibit sensitivity to the binding of a single molecule (with a conductance change of more than 100 nS for binding of a reactive carbodiimide), due to Coulomb interaction between the molecule and the defect that modulates scattering in the one-dimensional channel¹⁵. Compared with molecular-bridge devices, these devices can be prepared with much higher yield due to the real-time monitoring of conductance during defect generation. In this report, we take advantage of such defect-dominated conductance in nanotubes to produce measurements of DNA hybridization kinetics in which sufficiently high signal-to-noise ratio and bandwidth have been achieved to measure single-molecule kinetics and thermodynamics through a label-free field-effect-based approach.

Point-functionalized carbon nanotubes

Carbon nanotube transistors were fabricated using standard fabrication techniques. Nanotubes with diameters of less than 2 nm were grown by chemical vapour deposition¹⁶ on degenerately doped silicon wafers with 300 nm of thermally grown silicon oxide and contacted by multiple titanium electrodes using optical lithography. Oxygen plasma ion etching was used on a selectively exposed area in a second lithography step to electrically isolate neighbouring devices, leaving only one nanotube between a pair of electrodes. After fabrication, the devices were placed in an electrochemical cell, contacted by fixed wire bonds that were encapsulated with epoxy and sealed with a small glass tube. A platinum counter electrode was used in a pseudo-reference configuration to control the liquid potential both during oxidation and in subsequent aqueous experiments^{15,17}.

Point functionalization of the nanotubes was achieved similarly to the electrochemical method described previously¹⁴. An oxidation

¹Department of Electrical Engineering, Columbia University, New York, New York 10027, USA, ²Department of Chemistry, Columbia University, New York, New York 10027, USA, ³Department of Physics, Columbia University, New York, New York 10027, USA. *e-mail: shepard@ee.columbia.edu

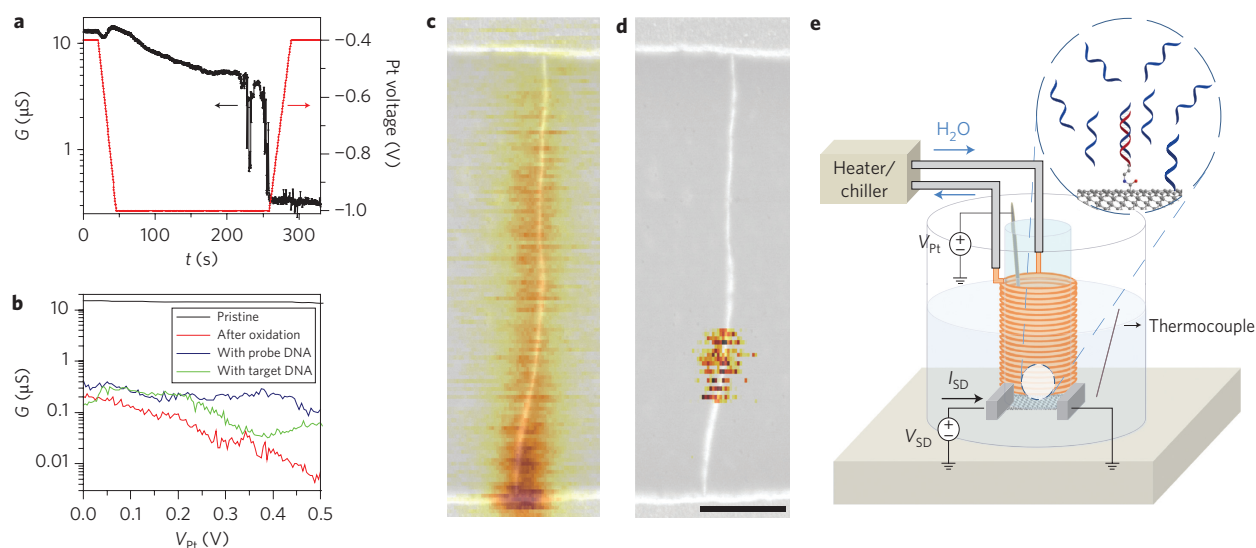


Figure 1 | Electrochemical oxidation of a carbon nanotube. **a**, Conductance-controlled oxidation of a nanotube in 1 M $\text{H}_2\text{SO}_4(\text{aq})$ with 30 mV bias. **b**, Conductance as a function of potential on the platinum electrode relative to the source-drain potential of the nanotube (V_{Pt}) at different stages in the process: before oxidation, after oxidation, after overnight coupling with probe DNA and after exposure to target DNA at 100 mV source-drain bias. Initially, the nanotube is metallic, but shows a large gate response after oxidation. **c,d**, Combined topography/SGM image of a semiconducting nanotube. Scale bar, 500 nm. In the overlaid SGM image, the darker yellow colour corresponds to lower current at a fixed bias voltage of 100 mV. Before oxidation (**c**), current is enhanced near the source where the Schottky barrier forms. After oxidation (**d**), the well localized region of highest sensitivity shows up in the middle of the tube, indicating the defect site. **e**, Schematic of the nanotube device (with an external circular heater/refrigerator to control temperature).

potential, slightly greater than the oxidation threshold (between -0.9 and -1 V), was applied through the platinum electrode in sulphuric acid (1 M H_2SO_4 in deionized water) until a sharp drop in the nanotube conductance to $\sim 10\%$ of the original conductance was observed. When we terminated oxidation at a 90% reduction in the conduction level, we found that 88% (23 of 26) of the devices remained conductive, of which 19% yielded functional single-molecule devices for use in measuring DNA hybridization kinetics. At a greater than 99% reduction in the conductance level¹⁴, the percentage of conductive devices decreased to 18% (7 of 38), of which 28% yielded functional single-molecule devices. We attribute the low yield in this final step to a number of factors, including the possibility that unreactive C–O and C=O defects were generated¹⁸, as well as multiple reactive defects and over-oxidation, which results in insulating devices. Figure 1a shows a typical conductance-controlled oxidation. Following the drop in device conductance, the oxidation potential is reduced and the device is immersed in 6.5 mM KMnO_4 to create a carboxyl functional group on the freshly created defect. Overall, we fabricated seven functional devices (from 64), which are characterized by the two-level conductance fluctuations described below when functionalized with probe DNA in the presence of complementary target.

We investigated the local defects generated by this process using scanning gate microscopy (SGM) of the nanotube before and after oxidation^{14,19}. By applying a local gate through the cantilever of an atomic force microscope (AFM) to a small region of the nanotube while monitoring the conductance, we could spatially map the sensitivity of the conductance to local gating. Figure 1c,d shows an SGM image overlaid with the device topography before and after oxidation, respectively. This device is a semiconducting nanotube, and Fig. 1c shows that the Schottky barriers²⁰ at the contacts dominate the gate sensitivity of the device. After oxidation, however, the sensitivity is localized to the location of the defect on the nanotube and no longer depends on the initial band structure. Both metallic and semiconducting nanotube devices have been used and they generally show large gate dependence after oxidation. A representative current/voltage (I – V) characteristic is shown in Fig. 1b for a device in its pristine state and after oxidation.

Electrical detection of DNA hybridization

These point-functionalized devices were used to study the kinetics and thermodynamics of DNA hybridization for two different 10-mer duplex DNAs with the experimental setup shown in Fig. 1e. Probe DNA, terminated with an amine group and a three-carbon linker at the 5' end was covalently attached to the carboxyl defect on the nanotube through a standard coupling reaction using sulpho-*N*-hydroxysuccinimide (sulpho-NHS) and 1-ethyl-3-(3-dimethylaminopropyl)carbodiimide (EDC). After thoroughly rinsing the device with deionized water, all subsequent measurements are carried out in phosphate buffered saline solution ($1\times$ PBS, pH = 7.4). After attaching the probe DNA to the point defect in the nanotube, the temperature was controlled with a thermal water bath (± 0.1 °C). When thermal equilibrium was reached (~ 10 min), we monitored the device conductance for periods of 30 s. Without the presence of target DNA, the devices show no particular features in a conductance dominated by flicker ($1/f$) noise, as shown in Fig. 2a. The intrinsic bandwidth of the device exceeded 10 kHz (see Supplementary Information), but we applied external measurement filters to reduce the bandwidth to 4 kHz for the measurements presented here. This resulted in an overall input-referred noise level of ~ 1 nA_{rms} at 100 mV source-to-drain bias (Supplementary Table S1).

When the device was immersed in buffer containing complementary target DNA, however, large-amplitude two-level fluctuations appear, as shown in Fig. 2c, with a conductance difference of ~ 60 – 100 nS and with a signal-to-noise ratio of better than three over the $1/f$ noise background for a time interval of 30 s, which could be improved by using shorter time intervals (Supplementary Fig. S10, S11, Table S1). The real-time conductance data of a representative device (Device 1) are shown with the probe DNA NH_2 -5'-GGAAAAAAGG-3' (probe A₆) and $1\ \mu\text{M}$ complementary target DNA. The two conductance states have a strong temperature dependence; the device is mostly in the low-conductance state at low temperature and in the high-conductance state both at high temperature and before the addition of target DNA. Around the melting temperature, the two states are similarly

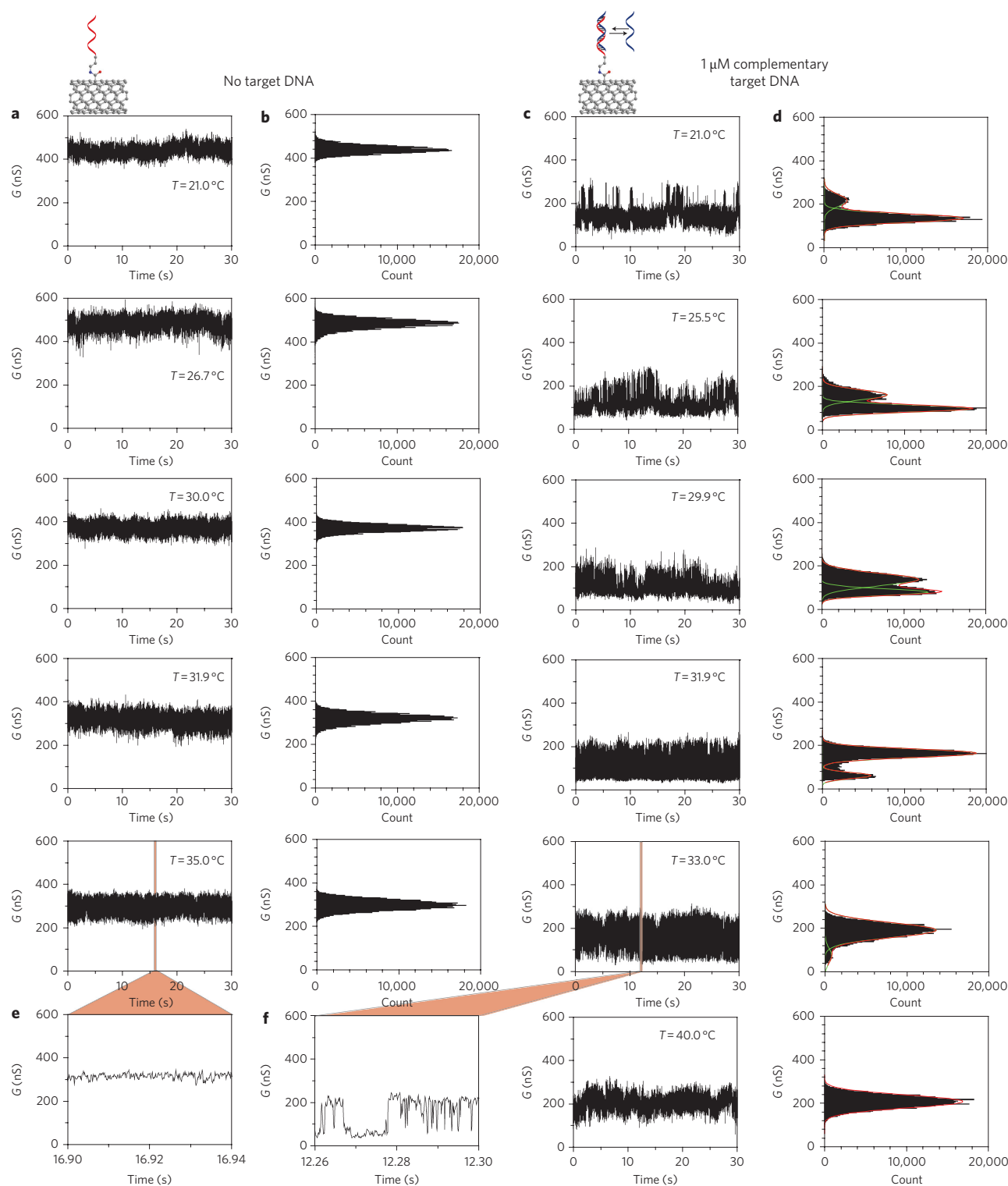


Figure 2 | Real-time measurements of DNA kinetics. **a**, Conductance recordings of Device 1 over one 30 s interval with DNA oligonucleotide probe $\text{NH}_2\text{-5'-GGAAAAAAGG-3'}$ (A_6) without exposure to complementary DNA target in $1\times$ PBS. The temperature is varied from 21 to 35 °C at a source-drain bias of 100 mV and zero V_{pt} . **b**, Conductance-based histograms of time intervals shown in **a**. **c**, Conductance recordings of Device 1 over a 30 s interval with DNA oligonucleotide probe $\text{NH}_2\text{-5'-GGAAAAAAGG-3'}$ (A_6) after exposure to complementary DNA target in $1\times$ PBS. **d**, Conductance-based histograms of time intervals shown in **c**. The two levels are fit to Gaussian distributions. **e,f**, Representative short time interval (40 ms) for real-time conductance recording for probe only and after exposure to complementary target DNA.

occupied. Owing to this evident temperature correlation, we propose a model in which the conductance is modulated by probe–target hybridization, consistent with other observations that target DNA binding to a covalently attached DNA probe reduces

tube conductance¹² due to increased scattering and charge transfer at the defect created by the target attachment. The low-conductance state represents a device with duplex DNA and the high-conductance state represents a device with unbound probe DNA. In

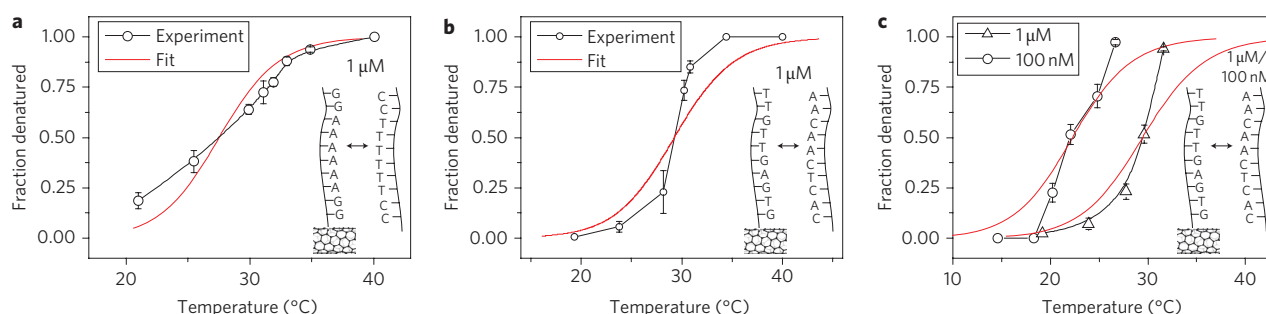


Figure 3 | DNA melting curves. **a**, Melting curve extracted from nanotube two-level fluctuations (Device 1) for probe DNA $\text{NH}_2\text{-5'-GGAAAAAAGG-3'}$ (A_6) and complementary target with van't Hoff fit. **b**, Melting curve extracted from nanotube two-level fluctuations (Device 2) for probe DNA $\text{NH}_2\text{-5'-GTGAGTTGTT-3'}$ (A_1) and complementary target with van't Hoff fit. **c**, Melting curve showing two different target concentrations (1 μM and 100 nM) with DNA probe $\text{NH}_2\text{-5'-GTGAGTTGTT-3'}$ (A_1) and complementary target with van't Hoff fit using Device 3. Error bars are calculated from at least eight different 30 s intervals at each temperature.

principle, longer DNA strands should increase scattering further and result in larger-amplitude fluctuations, but we expect that this effect would be partially offset by Debye screening from the dissolved solution counter-ions. The above model is further supported by the observation that these two-level fluctuations are not observed in pristine control devices without electrochemical modification either before or after the addition of target DNA (Supplementary Fig. S6) and control devices that have been linked with probe DNA with non-complementary target (Supplementary Fig. S8E). Note that there is a baseline drop in the conductance after DNA target is added, which we attribute to non-specific adsorption²¹.

We can relate the conductance modulation to a change in the transmission probability at the defect (using the Landauer-Büttiker formalism¹⁹) as

$$R_{\text{total}} = R_c + \frac{h}{4e^2} \left(1 + \frac{1-T}{T} \right)$$

where R_c is the resistance of the device before oxidation and T is the transmission probability through the defect. For this particular device $R_c = 53 \text{ k}\Omega$, and the transmission probability changes from 0.0055 before adding DNA target to ~ 0.0018 with target; that is, when the target DNA binds, the transmission probability is modulated by a factor of three. Neither AFM nor SGM techniques have sufficient spatial resolution to determine if the change in the device happens at a single carboxylate or if only a single DNA molecule covalently attaches to the nanotube. Multiple DNA probes could be attached to the nanotube, leading to multilevel fluctuation; however, because of the strong two-level fluctuations, we conclude that only a single DNA interaction dominates the conductance modulation, and the fluctuations are fit to a two-level model.

By taking the ratio of the areas under the low- and high-conductance state curves from the Gaussian fits in Fig. 2d, we obtain the melting curve shown in Fig. 3a. We also obtain melting curves of the same DNA duplex in solution through ultraviolet-visible absorption spectroscopy (UV-Vis) (Supplementary Fig. S9).

Assuming a two-state model where the DNA strands are either in single or duplex form, the equilibrium constant K in solution is given by $K = 2\alpha/(1-\alpha)^2C$ where α is the fraction of total strand concentration C that is in duplex form²². For surface-based hybridization, the equilibrium constant can be written as the Langmuir isotherm $K = \alpha/(1-\alpha)C$ (ref. 23). For both surface- and solution-based hybridization, we can then relate the temperature to the fraction of DNA in duplex form through the thermodynamic relation, $-RT \ln(K) = \Delta H^0 - T\Delta S^0$. The melting temperature of the DNA duplex (where $\alpha = 0.5$) as measured by the nanotube ($T_m = 27.5^\circ\text{C}$) is slightly lower and the transition is sharper compared to the free DNA ($T_m = 32.3^\circ\text{C}$). A similar observation has been made for DNA linked to gold nanoparticles²⁴ and RNA adsorbed to carbon nanotubes²⁵ due to interactions between the molecules and the surface²⁶. This is considered further below in the context of analysing the results of the kinetic studies.

Figure 3b,c shows the melting curves extracted for another probe, oligonucleotide $\text{NH}_2\text{-5'-GTGAGTTGTT-3'}$ (probe A_1). We show results for a nanotube device (Device 2) with 1 μM complementary target concentration (Fig. 3b) and another device (Device 3) with both 1 μM and 100 nM complementary target concentrations (Fig. 3c). We observe that the lower target concentration reduces the melting temperature, similar to what has been observed in bulk solution. We summarize the thermodynamic properties for both DNA strands and compare them to results with standard UV-Vis analysis in Table 1.

Single-molecule hybridization kinetics

To study the kinetics of DNA hybridization and gain further insight into the thermodynamics observed through time-averaging of a single-molecule system, we extracted (Fig. 4a) the dwell times in the high (τ_{high}) and low states (τ_{low}) in the presence of flicker noise by idealizing the transitions using a hidden Markov model (incorporated in the vbFRET software package)²⁷ that has been used in smFRET experiments to study conformational changes in biomolecules²⁸. The lifetime in each state was extracted by exponentially fitting the dwell-time histograms (Supplementary Figs S2,S5).

Table 1 | Thermodynamic properties of DNA hybridization comparing solution-based UV-Vis measurements and conductance-based single-molecule nanotube experiments.

DNA	Method	ΔH^0 (kJ mol ⁻¹)	ΔS^0 (J K ⁻¹ mol ⁻¹)	T_m at 1 μM (°C)	E_a (hybridizing) (kJ mol ⁻¹)	E_a (melting) (kJ mol ⁻¹)
Probe (A_6): $\text{NH}_2\text{-5'-GGAAAAAAGG-3'}$	Solution	384	1,134	32.3	—	—
Target: $3'\text{-CCTTTTTC-5'}$	Nanotube	313	923	27.5	-142	44/398
Probe (A_1): $\text{NH}_2\text{-5'-GTGAGTTGTT-3'}$	Solution	357	1,026	36.2	—	—
Target: $3'\text{-CACTCAACAA-5'}$	Nanotube	239	674	29.4	-202	225

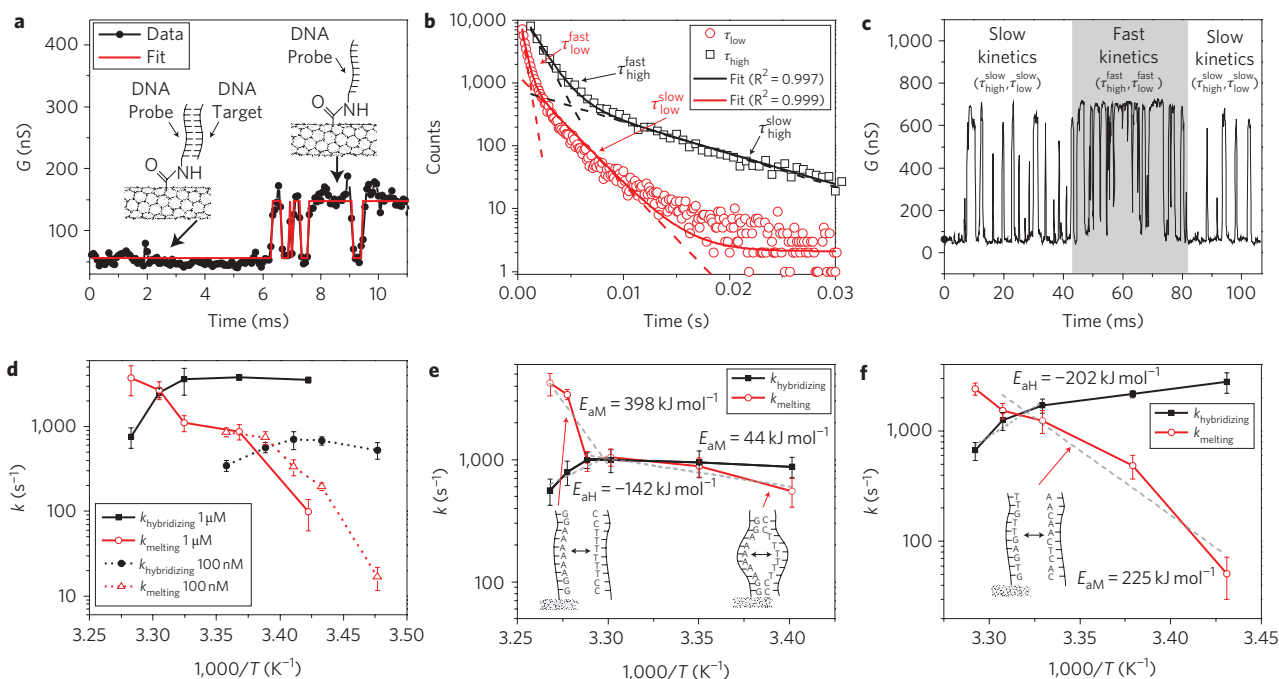


Figure 4 | DNA kinetics analysis. **a**, Conductance of Device 1 (Fig. 2a) showing experiment data and idealized fits resulting from hidden-Markov-model analysis using vbFRET. Inset: associated bound and unbound states of the probe DNA. **b**, Example of double exponential fitting at 1 μM target concentration and 32 $^{\circ}\text{C}$ showing both fast and slow lifetimes (Device 3). **c**, Conductance data, showing intervals with both fast and slow kinetics (Device 3). **d**, Arrhenius plot showing hybridizing and melting rates for 100 nM and 1 μM complementary target concentrations (Device 3). **e**, Arrhenius plot of Device 1 showing hybridizing and melting rates. A sharp transition in activation energy is shown around the melting temperature and is attributed to bubble kinetics at lower temperatures. **f**, Arrhenius plot of Device 2. There is no sharp transition in the activation energy. Error bars for the Arrhenius plots are calculated from at least sixteen different 15 s intervals.

From this lifetime analysis, we determined that the dwell-time histograms could be best fit by a double exponential function with time constants, $\tau_{\text{fast}}^{\text{low}} < \tau_{\text{fast}}^{\text{high}}$ and $\tau_{\text{slow}}^{\text{high}} < \tau_{\text{slow}}^{\text{low}}$ (Fig. 4b). The origin for the double exponential may be the result of two competing pathways for hybridization. Similar models have been used to describe DNA hybridization kinetics with immobilized probes on silicon or glass²⁹ and how proteins find specific target sites along DNA strands^{30,31}. In this model, target DNA reached the probe either by three-dimensional diffusion or non-specific adsorption followed by surface diffusion. As shown in Fig. 4c, the nanotube conductance switches between two distinct kinetic modes with different time constants. How these time constants are associated with solution- or surface-based kinetics is determined by examining the concentration dependence of the associated dwell times. From chemical kinetics, we expect the solution hybridization rate ($k_{\text{hybridizing}}$) to be proportional to DNA target concentration (bimolecular process), and the solution melting rate (k_{melting}) to be independent of concentration (unimolecular process). Figure 4d shows the Arrhenius plot for Device 3 with 100 nM and 1 μM complementary target concentration using $k_{\text{hybridizing}} = 1/\tau_{\text{fast}}^{\text{high}}$ and $k_{\text{melting}} = 1/\tau_{\text{slow}}^{\text{low}}$ for the 1 μM concentration and $k_{\text{hybridizing}} = 1/\tau_{\text{fast}}^{\text{low}}$ and $k_{\text{melting}} = 1/\tau_{\text{slow}}^{\text{high}}$ for the 100 nM concentration so that the hybridizing and melting rates behave as expected based on solution ensemble experiments and as described above. We believe that the target concentration at which $k_{\text{hybridizing}}$ (k_{melting}) goes from being determined by $\tau_{\text{fast}}^{\text{high}}$ ($\tau_{\text{fast}}^{\text{low}}$) to being determined by $\tau_{\text{slow}}^{\text{high}}$ ($\tau_{\text{slow}}^{\text{low}}$) depends on the ratio of one-dimensional and three-dimensional diffusion rates and the concentration dependence of the surface-based hybridization and melting rates (Supplementary Figs S14,S15).

Arrhenius plots for $k_{\text{hybridizing}}$ and k_{melting} at 1 μM for Devices 1 (probe A₆) and 2 (probe A₁) are presented in Fig. 4e and f, respectively. The Arrhenius plot of Device 2 (Fig. 4f) looks very similar to

those reported^{2,3} for DNA duplex kinetics studied with DNA hairpins. The melting rates (k_{melting}) follow Arrhenius-like behaviour and are very dependent on temperature, whereas the hybridization rates ($k_{\text{hybridizing}}$) have anti-Arrhenius behaviour and are only slightly temperature-dependent. This anti-Arrhenius behaviour yields a negative activation energy, which implies that the reaction rate decreases with increasing temperature and the free-energy barrier arises from a significant loss of entropy³². The slight curvature in the Arrhenius plot has also been observed with DNA hairpin hybridization³ and protein folding³³ and is attributed to a change in the rate-limiting step of the reaction as a function of temperature, because of a significant temperature dependence in either the activation entropy or enthalpy^{34,35}.

The Arrhenius plot of Device 1 (Fig. 4e) shows a remarkably different behaviour for k_{melting} , with a sharp change in activation energy around the melting temperature. At temperatures less than the melting temperature, k_{melting} has a small activation energy (44 kJ mol⁻¹) that can be seen from the shallow slope in the Arrhenius plot. We attribute this to breathing of the DNA duplex (probe A₆ for Device 1), which consists of six adenine–thymine (A–T) base pairs that are enclosed by guanine–cytosine (G–C) bases. This differs from the A₁ duplex (for Devices 2 and 3), which has at most two neighbouring A–T bases. We speculate that the fluctuations below the melting point for Device 1 could be due to bubble dynamics of the A–T region (which have been reported previously^{36,37}).

In addition to the solution and surface modes, we also observe occasional several-second-long non-ergodic time intervals when the fluctuations stop (Supplementary Fig. S13), which translate into long tails in the dwell-time histograms. This behaviour could be due to reversible states in which the DNA complex may adhere to the nanotube surface in a conformation that impedes the

binding kinetics. From the dwell-time histogram, we estimate the percentage of non-ergotic time intervals to be $\sim 10\%$ of the total monitored time.

In conclusion, we have presented a novel single-molecule label-free bioanalytical system capable of probing molecular kinetics at microsecond timescales. We expect this method to be powerful for the immediate exploration of applications in single-molecule studies with fast time resolution, such as label-free single-nucleotide polymorphism (SNP) detection and sequencing-by-synthesis (SBS). In addition, this methodology may prove powerful for single-molecule studies of protein folding and enzymatic activity. Future work will also involve incorporating these devices on active substrates with integrated measurement electronics to reduce both parasitic impedances and measurement noise so that we can probe kinetics at even higher rates and signal-to-noise ratios.

Methods

Device fabrication. The catalyst solution for nanotube growth was composed of *p*-methyl methylacetoxycalix[6]arene (MC6, Tokuyama Corp.) and Fe(III) acetylacetonate (Fe(Acac)₃, Aldrich) in monochlorobenzene¹⁶. A solution of 1.0 wt% MC6 and 0.1 wt% Fe(Acac)₃ was brushed onto one edge of a piranha-cleaned SiO₂ substrate (300 nm) and then subjected to a preheated (500 °C) furnace for 10 min in air to remove the resist. After flushing the system with argon at the same temperature for 10 min, the temperature was ramped to 750 °C and connected to the reducing gases of argon and hydrogen (642 s.c.c.m. and 115 s.c.c.m., respectively) to activate the iron nanoparticles for 1 h. Carbon nanotubes were then grown at 880 °C for 1 h by a chemical vapour deposition (CVD) process from the iron nanoparticles, using ethanol as the carbon source³⁸. The flow rates for growth were 138 s.c.c.m. for argon and 18 s.c.c.m. for hydrogen. In general, the nanotubes grown were several millimetres long and had a spacing of ~ 50 μm .

For device fabrication, nanotubes were grown on degenerately doped silicon substrates ($\rho = 0.01$ $\Omega\text{ cm}$) with a 300 nm thermally grown SiO₂ layer. Electrodes to the nanotubes were defined using optical lithography in a bilayer (120 nm LOR1A/1.3 μm Shipley S1813) resist, followed by electron-beam evaporation of a 75 nm titanium film and lift-off in PG Remover. Scanning electron microscopy and atomic force microscopy were used to locate the nanotubes relative to alignment marks and electrodes on the substrate and to measure their diameter (only tubes with a diameter less than 2 nm were chosen). Afterwards, another lithography step was used to cover a selected nanotube followed by an oxygen plasma etch (Technics Series 800 RIE machine, 50 W RF power, oxygen 250 mTorr for 10 s) to remove all other nanotubes. This etching step was crucial, because it guaranteed that only a single tube bridged the electrodes and that neighbouring electrodes were electrically isolated (Supplementary Fig. S1A,S1B). After fabrication, the substrates were annealed in forming gas (a mixture of hydrogen and argon) for at least 2 h at 400 °C to remove the resist residue completely (Supplementary Fig. S1C,S1D)³⁹.

Measurement instrumentation and device oxidation. After wire-bonding the chips to 44-pin J-leaded chip carriers (Chelsea Technology), the wirebonds were electrically and mechanically insulated by standard epoxy (EPO-TEK GE120 and EPO-TEK 302-3M for damming and filling). A small glass tube was fixed on top of the epoxy to create a 3 ml cavity for the aqueous experiments. A platinum wire in a pseudo-reference configuration was used to modulate the liquid gate potential while the back gate was held at zero potential. We have also run the experiment with an Ag/AgCl electrode both in a pseudo-reference configuration and a potentiostat configuration (using both the platinum and Ag/AgCl electrode in a feedback system) and have determined that the choice of electrode does not affect the results. The advantage of a platinum electrode lies in the fact that it can withstand the harsh electrochemical environment and that it can be cleaned easily between experiments by grinding away the outer layer with fine sandpaper and then rinsing it with deionized water.

For the conductance plots as a function of gate voltage, we used an Agilent 4155C Semiconductor Parameter Analyzer to sweep the electrolyte gate while monitoring the conductance in a two-probe configuration with 100 mV source-to-drain bias. The gate leakage was always negligible (< 1 nA) with respect to the source-drain current. This was a good indication that the native oxide of the titanium electrodes sufficiently reduced any electrochemical leakage currents. Real-time experiments were monitored with a Labview program. A voltage source (Keithley 2400 Source Meter) was used to set the electrolyte voltage while the conductance through a selected device was monitored with a transimpedance current amplifier (Stanford Research SR570) that was sampled at either 10 kHz or 15 kHz using a NIDAQ card. The transimpedance amplifier also set the source drain voltage to 100 mV and the bandwidth was 4 kHz (at 200 nA V⁻¹ sensitivity, 10 kHz/12 dB low-pass filter). Devices that had been oxidized in sulphuric acid (1 M H₂SO₄(aq)) were connected to a second voltage source that was always kept 0.4 V above the platinum potential to avoid further oxidation or accidental

reduction. This allowed several devices to be oxidized simultaneously. Afterwards, we flushed the glass chamber with deionized water (while keeping the potential fixed) and then immersed the devices in 6.5 mM potassium permanganate (KMnO₄(aq)) for 45 s.

DNA functionalization. The carboxylate defects created in the nanotube during the oxidation process were covalently linked to the DNA in a two-step process⁴⁰. First, the carboxylic acid group in the nanotube was activated for 30 min in MES-buffered saline solution (pH = 4.7, Pierce Biotechnology) with 1 mM EDC (1-ethyl-3-[3-dimethylaminopropyl]carbodiimide hydrochloride) and 2 mM Sulpho-NHS (N-hydroxysulphosuccinimide) (Pierce Biotechnology). The devices were then rinsed with fresh buffer solution, followed by rinsing in 1 \times PBS buffer (pH = 7.4). We then incubated the devices in 2 μM single-stranded probe DNA with an amine group at the 5' end in 1 \times PBS buffer (pH = 7.4) with 1 mM EDC and 2 mM Sulpho-NHS overnight (14 h). The devices were then rinsed with deionized water and immersed in 1 \times PBS for further characterization.

Scanning gate microscopy. SGM was carried out with a Park Systems Corp. XE-100 AFM using a Cr/Au tip (NSC 14-Cr/Au) at room temperature. SGM and electron force microscopy (EFM) were implemented concurrently, and the tip was lifted to 30 nm above the nanotube. For SGM, a small 50 mV bias was applied across the nanotube using a lock-in amplifier (Stanford Research SR830) and the tip was biased at -2 V. The device was slightly p-type (Supplementary Fig. S8), and this negative bias increased the conductance through local tip gating. Both the topography image and the SGM image were levelled, but no further processing was carried out. The conductance of the pristine device increased by $\sim 8\%$ when the tip was over the Schottky barrier, whereas the conductance of the point-functionalized device increased by more than 22% when the tip was over the defect.

Received 17 August 2010; accepted 9 December 2010;
published online 23 January 2011

References

- Bonnet, G., Krichinsky, O. & Libchaber, A. Kinetics of conformational fluctuations in DNA hairpin-loops. *Proc. Natl Acad. Sci. USA* **95**, 8602–8606 (1998).
- Li, H. T., Ren, X. J., Ying, L. M., Balasubramanian, S. & Klenerman, D. Measuring single-molecule nucleic acid dynamics in solution by two-color filtered ratiometric fluorescence correlation spectroscopy. *Proc. Natl Acad. Sci. USA* **101**, 14425–14430 (2004).
- Wallace, M. I., Ying, L., Balasubramanian, S. & Klenerman, D. Non-Arrhenius kinetics for the loop closure of a DNA hairpin. *Proc. Natl Acad. Sci. USA* **98**, 5584–5589 (2001).
- Deniz, A. A., Mukhopadhyay, S. & Lemke, E. A. Single-molecule biophysics: at the interface of biology, physics and chemistry. *J. R. Soc. Interface* **5**, 15–45 (2008).
- Fei, J., Kosuri, P., MacDougall, D. D. & Gonzalez, R. L. Jr Coupling of ribosomal L1 stalk and tRNA dynamics during translation elongation. *Mol. Cell* **30**, 348–359 (2008).
- Patolsky, F. *et al.* Electrical detection of single viruses. *Proc. Natl Acad. Sci. USA* **101**, 14017–14022 (2004).
- Armani, A. M., Kulkarni, R. P., Fraser, S. E., Flagan, R. C. & Vahala, K. J. Label-free, single-molecule detection with optical microcavities. *Science* **317**, 783–787 (2007).
- Burg, T. P. *et al.* Weighing of biomolecules, single cells and single nanoparticles in fluid. *Nature* **446**, 1066–1069 (2007).
- Hughes, R. C., Ricco, A. J., Butler, M. A. & Martin, S. J. Chemical microsensors. *Science* **254**, 74–80 (1991).
- Cecconi, C., Shank, E. A., Bustamante, C. & Marqusee, S. Direct observation of the three-state folding of a single protein molecule. *Science* **309**, 2057–2060 (2005).
- Besteman, K., Lee, J. O., Wiertz, F. G. M., Heering, H. A. & Dekker, C. Enzyme-coated carbon nanotubes as single-molecule biosensors. *Nano Lett.* **3**, 727–730 (2003).
- Star, A. *et al.* Label-free detection of DNA hybridization using carbon nanotube network field-effect transistors. *Proc. Natl Acad. Sci. USA* **103**, 921–926 (2006).
- Guo, X., Gorodetsky, A. A., Hone, J., Barton, J. K. & Nuckolls, C. Conductivity of a single DNA duplex bridging a carbon nanotube gap. *Nature Nanotech.* **3**, 163–167 (2008).
- Goldsmith, B. R. *et al.* Conductance-controlled point functionalization of single-walled carbon nanotubes. *Science* **315**, 77–81 (2007).
- Goldsmith, B. R., Coroneus, J. G., Kane, A. A., Weiss, G. A. & Collins, P. G. Monitoring single-molecule reactivity on a carbon nanotube. *Nano Lett.* **8**, 189–194 (2008).
- Ishida, M., Hongo, H., Nihey, F. & Ochiai, Y. Diameter-controlled carbon nanotubes grown from lithographically defined nanoparticles. *Jpn J. Appl. Phys.* **2** **43**, L1356–L1358 (2004).
- Chen, R. J. *et al.* Noncovalent functionalization of carbon nanotubes for highly specific electronic biosensors. *Proc. Natl Acad. Sci. USA* **100**, 4984–4989 (2003).

18. Kosynkin, D. V. *et al.* Longitudinal unzipping of carbon nanotubes to form graphene nanoribbons. *Nature* **458**, 872–876 (2009).
19. Bachtold, A. *et al.* Scanned probe microscopy of electronic transport in carbon nanotubes. *Phys. Rev. Lett.* **84**, 6082–6085 (2000).
20. Freitag, M. *et al.* Imaging of the Schottky barriers and charge depletion in carbon nanotube transistors. *Nano Lett.* **7**, 2037–2042 (2007).
21. Minot, E. D. *et al.* Carbon nanotube biosensors: the critical role of the reference electrode. *Appl. Phys. Lett.* **91**, 093507 (2007).
22. Borer, P. N., Dengler, B., Tinoco, I. Jr & Uhlenbeck, O. C. Stability of ribonucleic acid double-stranded helices. *J. Mol. Biol.* **86**, 843–853 (1974).
23. Gong, P. & Levicky, R. DNA surface hybridization regimes. *Proc. Natl Acad. Sci. USA* **105**, 5301–5306 (2008).
24. Sun, Y., Harris, N. C. & Kiang, C. H. Melting transition of directly linked gold nanoparticle DNA assembly. *Physica A* **350**, 89–94 (2005).
25. Karachevtsev, V. A. *et al.* Adsorption of poly(rA) on the carbon nanotube surface and its hybridization with poly(rU). *ChemPhysChem* **9**, 2010–2018 (2008).
26. Brewood, G. P. *et al.* Electrical detection of the temperature induced melting transition of a DNA hairpin covalently attached to gold interdigitated microelectrodes. *Nucleic Acids Res.* **36**, e98 (2008).
27. Bronson, J. E., Fei, J., Hofman, J. M., Gonzalez, R. L. Jr & Wiggins, C. H. Learning rates and states from biophysical time series: a Bayesian approach to model selection and single-molecule FRET data. *Biophys. J.* **97**, 3196–3205 (2009).
28. Fei, J. *et al.* Allosteric collaboration between elongation factor G and the ribosomal L1 stalk directs tRNA movements during translation. *Proc. Natl Acad. Sci. USA* **106**, 15702–15707 (2009).
29. Chan, V., Graves, D. J. & McKenzie, S. E. The biophysics of DNA hybridization with immobilized oligonucleotide probes. *Biophys. J.* **69**, 2243–2255 (1995).
30. von Hippel, P. H. & Berg, O. G. Facilitated target location in biological systems. *J. Biol. Chem.* **264**, 675–678 (1989).
31. Halford, S. E. & Marko, J. F. How do site-specific DNA-binding proteins find their targets? *Nucleic Acids Res.* **32**, 3040–3052 (2004).
32. Ansari, A., Kuznetsov, S. V. & Shen, Y. Configurational diffusion down a folding funnel describes the dynamics of DNA hairpins. *Proc. Natl Acad. Sci. USA* **98**, 7771–7776 (2001).
33. Oliveberg, M., Tan, Y. J. & Fersht, A. R. Negative activation enthalpies in the kinetics of protein folding. *Proc. Natl Acad. Sci. USA* **92**, 8926–8929 (1995).
34. Dobson, C. M., Sali, A. & Karplus, M. Protein folding: a perspective from theory and experiment. *Angew. Chem. Int. Ed.* **37**, 868–893 (1998).
35. Chalikian, T. V., Volker, J., Plum, G. E. & Breslauer, K. J. A more unified picture for the thermodynamics of nucleic acid duplex melting: a characterization by calorimetric and volumetric techniques. *Proc. Natl Acad. Sci. USA* **96**, 7853–7858 (1999).
36. Altan-Bonnet, G., Libchaber, A. & Krichevsky, O. Bubble dynamics in double-stranded DNA. *Phys. Rev. Lett.* **90**, 138101 (2003).
37. Metzler, R., Ambjornsson, T., Hanke, A. & Fogedby, H. C. Single DNA denaturation and bubble dynamics. *J. Phys. Condens. Matter* **21**, 034111 (2009).
38. Huang, L. M., Cui, X. D., White, B. & O'Brien, S. P. Long and oriented single-walled carbon nanotubes grown by ethanol chemical vapor deposition. *J. Phys. Chem. B* **108**, 16451–16456 (2004).
39. Ishigami, M., Chen, J. H., Cullen, W. G., Fuhrer, M. S. & Williams, E. D. Atomic structure of graphene on SiO₂. *Nano Lett.* **7**, 1643–1648 (2007).
40. Hermanson, G. T. *Bioconjugate Techniques* 2nd edn (Academic Press, 2008).

Acknowledgements

This work was supported in part by the National Science Foundation (grants ENG-0707748 and CHE-0641523). Additional support was provided by the New York State Office of Science, Technology, and Academic Research (NYSTAR). This work was also supported in part by the Office of Naval Research (grants N00014-09-01-0250 and N00014-09-1-1117) and by the National Institutes of Health (grant R33-HG003089).

Author contributions

S.S., C.-Y.C. and K.L.S. designed the experiments. S.S. and C.-Y.C. performed the experiments and analysed the data. Y.-J.Y. and P.K. assisted in the AFM and SGM experiments. C.N. and R.L.G. assisted with data analysis. S.S., C.-Y.C. and K.L.S. co-wrote the paper. All authors discussed the results and commented on the manuscript.

Additional information

The authors declare no competing financial interests. Supplementary information accompanies this paper at www.nature.com/naturenanotechnology. Reprints and permission information is available online at <http://npg.nature.com/reprintsandpermissions/>. Correspondence and requests for materials should be addressed to K.L.S.